Observation of noise correlated by the Hawking effect in a water tank

L.-P. Euvé,[1] F. Michel,[2] R. Parentani,[2] T. G. Philbin,[3] and G. Rousseaux[1]

[1]*Institut Pprime, UPR 3346, CNRS-Université de Poitiers-ISAE ENSMA 11 Boulevard Marie et Pierre Curie-Téléport 2, BP 30179, 86962 Futuroscope Cedex, France*

[2]*Laboratoire de Physique Théorique, CNRS, Univ. Paris-Sud, Université Paris-Saclay, 91405 Orsay, France*

[3]*Physics and Astronomy Department, University of Exeter, Stocker Road, Exeter EX4 4QL, UK*

We measure the power spectrum and two-point correlation function for the fluctuating free surface on the downstream side of a stationary flow above an obstacle with high Froude number $F \approx 0.85$. On such a flow the scattering of incident long wavelength modes is analogous to that responsible for black hole radiation (the Hawking effect). Our measurements of the correlations clearly indicate a steady conversion of incident modes into pairs of modes of opposite energies. We then use a wave maker to measure the scattering coefficients responsible for this effect.

The Hawking effect in laboratory analogues of event horizons [1] has been well studied theoretically [2–4] and experiments have been performed in different systems [5–11]. Analogue horizons are created when waves propagate in a stationary counter-flowing medium: at points where the flow speed reaches that of the wave, the latter is blocked and converted to other branches of the dispersion relation. At low frequency, this gives rise to a mode amplification (an over-reflection [12]) which involves a negative energy wave [5, 13–15], and which is at the root of the Hawking effect [16]. Importantly, the scattered waves of opposite energy are correlated with each other [17]. As a result, when dealing with a noisy system, the two-point correlation function of the fluctuating quantity displays specific patterns both in space-time and in Fourier space [18–22].[1] We here consider surface waves on a stationary counter-current of water in a linear tank. Our work is inspired by the theoretical Refs. [14, 24–26] and builds on the experiments [5, 9, 27, 28].

Ignoring the surface tension, and assuming that the flow is incompressible and irrotational, the dispersion relation which relates the angular frequency ω and the wave-vector k is

$$(\omega - Uk)^2 = gk \tanh(kh), \tag{1}$$

where U is the flow velocity, h the water depth, and g the gravitational acceleration. In a flow to the right, i.e., $U > 0$, for a fixed ω, the three roots k_I, k_B, and k_H describe counter-propagating waves moving left relative to the fluid [4, 5, 14], while k_R describes a co-propagating mode, see Fig. 1. There are also transverse modes, which have an effective mass [29] proportional to their transverse wave-vector.

In stationary inhomogeneous flows, such as that of Fig. 2, ω is conserved. For fixed $\omega > 0$, the roots k_I and k_B merge at a point in the tank where U becomes sufficiently large [26]. This merging describes an incident long-wavelength mode I coming from the right, that is blue-shifted into a B mode with opposite group velocity $d\omega/dk$ (the slope of the curves in Fig. 1): the well-known wave blocking [14, 30]. For sufficiently low ω, it is accompanied by a non-adiabatic effect which generates an additional mode with wave vector k_H. This mode has a negative frequency $\omega - Uk$ as measured in the fluid frame, see Fig. 1, and thus carries a negative energy [5, 13–15]. Because the total wave energy is conserved, this conversion implies an amplification of the B mode. This is in strict analogy with the Hawking effect. [2]

The effect just described can be stimulated by an incident wave I generated by a wave maker, as was done in [5, 9]. In contrast, the quantum Hawking effect, of fundamental interest for black holes [16], arises from the amplification of vacuum fluctuations and gives rise to pairs of *correlated* quanta with opposite energy [17]. Surface waves in the water tank are not suitable to observe the quantum Hawking effect. But just as the quantum vacuum provides a horizon with an irreducible input, there is a background noise of surface waves in the inhomogeneous flow created by both the turbulent flow and the underwater obstacle, see Fig. 1 lower panel. Because of the mode conversion near the blocking point, this noise should be steadily *correlated*. In our experiment, we measured correlations among various modes in the downstream homogeneous region, see Fig. 2. Because the flow is stationary, these correlations are non-vanishing when the k_a's are evaluated at the same value of ω [19, 20, 22], see Fig. 3.

Our experiments were performed in the water channel of the Pprime Institute. The channel is 6.8 m long and 0.39 m wide. A PCM Moineau pump creates the water current and its flow rate is regulated by a variator. The water is first injected into a convergent chamber whose geometry and honeycomb structure produce an outgoing flow devoid of practically all boundary-layer effects and macro-vortices. At the downstream end of the channel, there is a guillotine which can be

[1] Observation of density correlations stemming from vacuum fluctuations was reported in a flowing atomic Bose condensate [23] while we were finishing this work.

[2] The "subluminal" relation of Eq. (1) implies that higher flow speeds are required to block lower frequency waves. It is difficult experimentally to have a flow that will block waves at all frequencies and in experiments to date [5, 9, 28] only waves above a critical frequency $\omega_{\min}$ were (essentially) blocked. Below $\omega_{\min}$, the incident mode is mostly transmitted over the obstacle, although there is still some partial conversion into the modes R, B, and H [26, 28]. Above $\omega_{\min}$, the main effect is the conversion into B and H. This effect was observed in [9] both below and above $\omega_{\min}$.

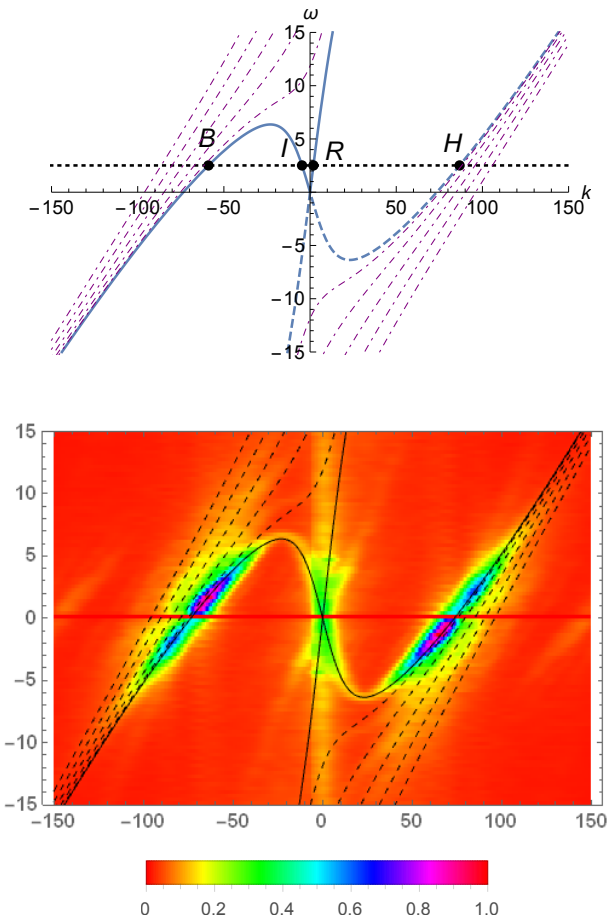

FIG. 1. Top: Dispersion relation in the homogeneous flow on the downstream side of the obstacle. k is in m^{-1} and ω in Hz. The effective parameters (see text below Eq. (2) for definition) are $U_{\mathrm{eff}} = 0.37\,\mathrm{m.s}^{-1}$ and $h_{\mathrm{eff}} = 88$ mm. The blue continuous (dashed) lines correspond to Eq. (1) with positive (negative) $\omega - Uk$. The four dots labelled by B, I, R, H give the roots k_a for a fixed $\omega > 0$ indicated by a dotted horizontal line. Purple, dot-dashed lines describe transverse modes with an even number of nodes in the transverse direction (those with an odd number are not detected by our experimental setup). Bottom: Square root of the power spectrum $\mathcal{P}(\omega, k)$ (divided by its maximum value) of the noise measured on the downstream side of the obstacle. The bright vertical line at $k \approx 0$ is an artefact coming from the vanishing of the normalisation factor S_k used in Eq. (2) at $k = 0$.

set in vertical motion around a mean height to generate a wave that propagates upstream, see Fig. 1 in [28]. To measure the free surface, as in [9, 27], a laser sheet was projected from above along the center line of the channel. A fluorescent dye was added to the water to obtain a laser line on the surface (non-penetration of the laser light into the fluid). Three cameras (Jai CVM2 1600x1200) captured this laser line, on a visualization window which is 2.16 m wide. Their resolution is 0.45 mm/px. We used a sub-pixel detection method similar to that of [9] with an accuracy of 0.1 mm, see also [27]. For more details, see Supplemental Material.

The obstacle used to obtain an inhomogeneous flow was de-

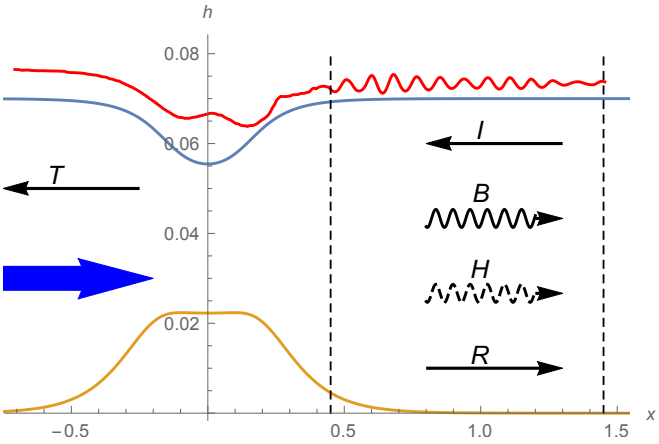

FIG. 2. Plots of the obstacle (bronze) and the observed free surface (red) in meters. The two dashed vertical lines indicate the region used to study the fluctuations of the free surface δh. The blue, thick arrow shows the direction of the flow. Thin arrows show the direction of propagation of the various modes produced by the scattering of the incident I mode. The letters I, B, H, R have the same meaning as in Fig. 1. The T arrow represents the transmitted wave in the upstream side. The blue curve gives the free surface chosen for determining the obstacle, see text for explanation.

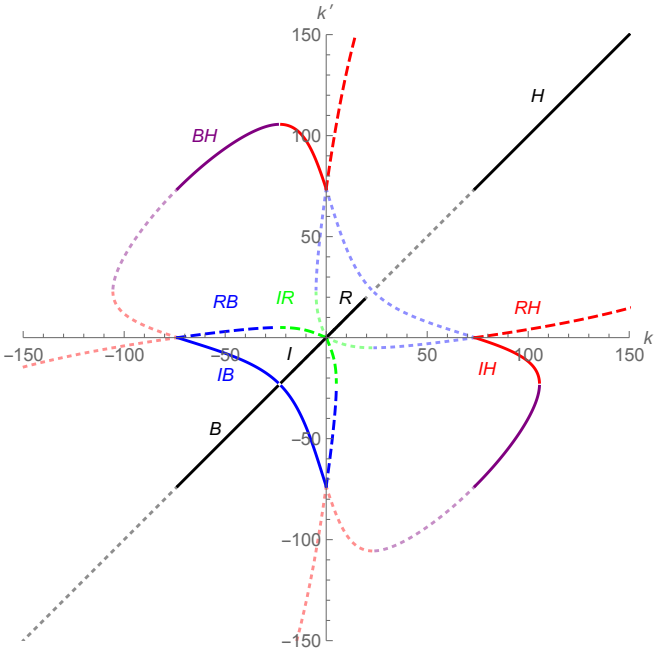

FIG. 3. Here we show the loci where k, k' are two roots of Eq. (1) for $\omega \in \mathbb{R}^+$ in a flow with same parameters as in Fig. 1. The oblique black segments show $k = k'$ for the four modes B, I, R, H. The three continuous curves show $\{k, k'\} = \{k_I, k_B\}$ (blue), $\{k_I, k_H\}$ (red), $\{k_B, k_H\}$ (purple), while the dashed lines $\{k_I, k_R\}$ (green), $\{k_R, k_B\}$ (blue), and $\{k_R, k_H\}$ (red), involve the mode k_R. Dotted lighter shaded curves correspond to $\omega < 0$. They are obtained from correlations with positive ω by $(k, k') \to (-k, -k')$.

signed following the procedure outlined in appendix A of [26]. It relies on the hodograph transformation for a 2D inviscid, irrotational, incompressible flow [31]. The shape of the obstacle is determined by the profile of the free surface, the asymptotic water depth, and flow velocity, see Fig. 2. The main advantage of this obstacle over the one used in [9, 28] is that it supports a flow with a relatively large Froude number (0.86 ± 0.03 in the present experiment instead of 0.67 ± 0.02). In addition, it produces a smaller static surface deformation, or undulation [15, 32], with a peak-to-peak amplitude of a few millimeters. The descending slope of the obstacle also has a larger maximum gradient: the slope of $c - U$, giving the analogue surface gravity in transcritical flows [26], has a maximum of 2 Hz instead of 1.2 Hz as used in [9] (here $c = \sqrt{gh}$ is the velocity of long-wavelength waves in the fluid frame).

We measured the fluctuations of the water height $\delta h(x,t)$, defined as the deviation from the time-averaged value of $h(x,t)$, in the downstream constant-flow region shown in Fig. 2. The upstream water height was taken to be $h_{\rm up} = 74$ mm, and the current was 8.97 Ls^{-1}. The upstream value of the flow velocity was thus $U_{\rm up} = 0.31\,{\rm ms}^{-1}$. As a first characterization of the noise, we studied the power spectrum

$$\mathcal{P}(\omega,k) \equiv \left\langle \left| \delta\tilde{h}(\omega,k) \right|^2 \right\rangle \times S_k^{-2}. \qquad (2)$$

(For former studies of the noise, see Ref. [27, 33]). Here, $\delta\tilde{h}(\omega,k)$ is the Fourier transform of $\delta h(t,x)$ and $S_k = |gk\tanh(kh)|^{1/4} \times |dk/d\omega|^{1/2}$ is the structure factor relating $\tilde{\delta h}$ to unit norm modes when working at fixed ω [15, 26]. (When evaluated along the a branch of the dispersion relation, $\mathcal{P}(\omega, k_a(\omega))$ gives the classical equivalent of the *mean* number of quasi-particles [21, 23], i.e., $\mathcal{P}(\omega, k_a(\omega)) \times \omega$ is proportional to the wave energy.) The Fourier transform in time is computed using a rectangular window, while we used a Hamming window function [34] with support $x \in [0.45{\rm m}, 1.45{\rm m}]$ to compute the spatial transform. The mean value is computed by dividing the data into 80 pieces of equal duration 12.5 s and averaging over them. The square root of $\mathcal{P}(\omega,k)$ is shown in the lower panel of Fig. 1. The dispersion relation of Fig. 1 has been drawn with the effective values $h_{\rm eff} = 88$ mm and $U_{\rm eff} = 0.37{\rm ms}^{-1}$ which have been chosen to match the observed wave numbers. The agreement is clear for all values of ω. We expect that the differences with $h_{\rm up}$ and $U_{\rm up}$ are due to boundary-layer, vorticity and turbulent effects.

To further characterize the noise, we measured the two-point correlation function

$$G_2(\omega;k,k') \equiv \left| \left\langle \delta\tilde{h}(\omega,k)\delta\tilde{h}(\omega,k')^* \right\rangle \right| \times (S_k S_{k'})^{-1}. \qquad (3)$$

In the upper plots of Fig. 4, we show $G_2(\omega;k,k')$ in the (k,k') plane for two positive frequencies: $\omega = 0.6$ and 2.5 Hz. We notice that the B and H modes of opposite energy are well correlated. Moreover, using the effective values $h_{\rm eff}$ and $U_{\rm eff}$ their location in the k,k' plane are in close agreement with the theoretical predictions of Fig. 3. On the right upper plot, we see that long-wavelength modes I and R are correlated with both B and H modes.

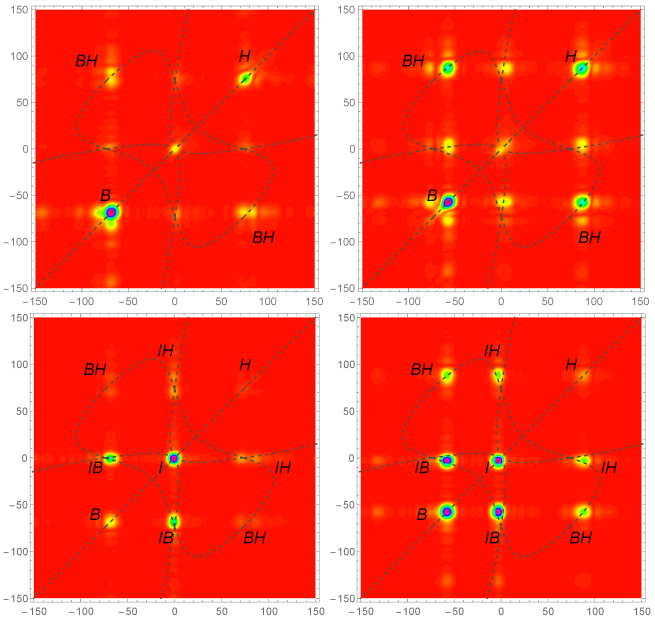

FIG. 4. In the upper row, we show the noise correlation function of Eq. (3) for $\omega = 0.6$ Hz (left) and 2.5 Hz (right). The color scale is the same as in Fig. 1. Dashed lines show the dispersion relation in the (k,k') plane, see Fig. 3. The letters B and H designate the power of the short wave length modes with opposite energies, and BH their correlations. In the lower row, we show again Eq. (3) when the wave-maker is sending the incident wave I for the corresponding frequencies. The IB and IH correlations are clearly visible.

To quantify the strength of the correlations we study

$$g_2(\omega;a,b) \equiv \frac{G_2(\omega;k_a,k_b)}{\sqrt{G_2(\omega;k_a,k_a)G_2(\omega;k_b,k_b)}}, \qquad (4)$$

where $k_a(\omega), k_b(\omega)$ are two solutions of the dispersion relation at fixed ω. For any statistical ensemble, g_2 is necessarily smaller than 1. It involves the classical counterparts of the two quantities which are used in quantum settings to assert that the state is entangled [20–23]. Figure 5 shows $g_2(\omega;a,b)$ as a function of ω for different modes. We notice that the BH correlations are strong since $g_2(\omega;B,H)$ is close to 1 except close to $\omega = \omega_{\rm min} \approx 0.8$ Hz and $\omega = \omega_{\rm max} \approx 5$ Hz (at which k_I and k_B merge in the asymptotic region). This indicates that B and H modes are mostly produced in BH pairs. IH correlations are much smaller, staying below 0.3 over most of the frequency domain. This implies that most of the BH pairs do not come from observed I modes with no transverse wave number. It probably means that a significant fraction of BH pairs have a non-vanishing transverse wave number. (At present we are not able to separate the contributions of B and H modes with and without transverse wave number, as the corresponding curves on the dispersion relation are very close to each other, see Fig. 1.) Some BH pairs should also be produced by *incident* waves H and R from the left. This

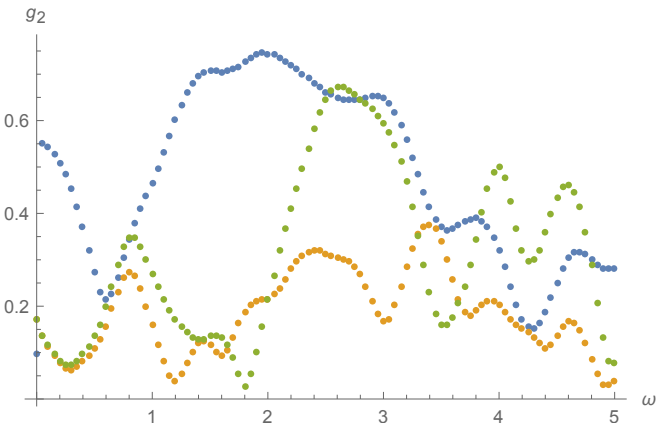

FIG. 5. As a function of the frequency, we represent the relative strength of the noise correlations of Eq. (4) between modes of opposite energies: in blue BH correlations, in green RH ones, and in bronze IH ones. We estimate that the uncertainties are of order 0.1.

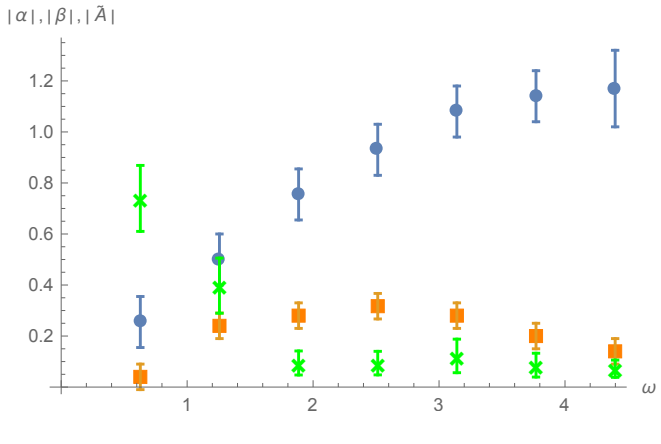

FIG. 6. Plots of the norm of the scattering coefficients $|\alpha|$ (blue circles), $|\beta|$ (orange squares), and $|\tilde{A}|$ (green crosses) observed when sending I waves for seven different frequencies. For $|\alpha|$ and $|\beta|$, error bars arise from the extension in k space over the finite integration window of 0.95m. Relative statistical uncertainties are smaller than 10% and do not contribute significantly. The transmission coefficient $\tilde{A}$ was obtained by a method similar to that of [28] and averaged over the 80 realizations. Here, error bars show the standard deviation.

possibility is reinforced by the fact that the RH correlations are in general larger than the IH ones. In addition, not all the incident I-mode noise is taken into account if some of it is generated by fluctuations in the region $x < 0.45$m. An effective description of this generation could be obtained from adapting to the present case the driven-damped wave equation of Ref. [35].

The scattering can be more accurately studied when sending a I wave towards the obstacle, with an amplitude significantly larger than the mean one of the noise, as done in [5, 9]. The corresponding values of G_2 are shown in the lower plots of Fig. 4. In the left plot, the autocorrelation (the power) of the incident wave dominates G_2. This was expected as $\omega < \omega_{\rm min}$ implies that the incident wave is essentially transmitted. In the right plot, $\omega > \omega_{\rm min}$, the power of the B wave is close to that of the incident one, as expected from the validity of the WKB approximation in this regime [4]. The negative-energy H wave remains relatively small in amplitude. However, HI and HB correlations are clearly visible, showing that it is produced by the analogue Hawking effect.

In Fig. 6 we show the norms of the coefficients α, β, and $\tilde{A}$ entering in the scattering of the (unit norm) incoming mode ϕ_I into the four outgoing modes [26], see Fig. 2,

$$\phi_I \to \alpha\,\phi_B + \beta\,\phi_H + A\,\phi_R + \tilde{A}\,\phi_T. \qquad (5)$$

The most accurate way we found to measure α and β consists in using the constructive interferences of the G_2 of Eq. (3):

$$|\alpha| = \frac{G_2(\omega, k_I, k_B)}{G_2(\omega, k_I, k_I)}, \quad |\beta| = \frac{G_2(\omega, k_I, k_H)}{G_2(\omega, k_I, k_I)}. \qquad (6)$$

In agreement with [26], for $\omega \leq \omega_{\rm min} \sim 0.8$Hz, $|\alpha|$ and $|\beta|$ both decrease whereas the transmission coefficient $|\tilde{A}|$ becomes large [28]. For $\omega > \omega_{\rm min}$, $|\alpha|$ increases and saturates to a value close to 1. $|\beta|$ also increases and then slowly decreases.

To understand this slow decrease, which was not found in [26], we performed new simulations taking the undulation into account more accurately, as was done in [36]. They indicate that the scattering on the undulation can explain the behavior of β shown in Fig 6. We have not succeeded in measuring the coefficient A relating long wavelength modes. Simulations indicate that it should be smaller than 0.2. Collecting the data, and assuming that $|A| \lesssim 0.2$, the unitarity relation $1 = |\alpha|^2 - |\beta|^2 + |A|^2 + |\tilde{A}|^2$ expressing the conservation of the norm [26] is obeyed within error bars.

To summarize, we observed the statistical properties of the water depth fluctuations downstream from an obstacle in a flow with a large maximum Froude number. Using the two-point correlation function in momentum space, we found that waves are produced in pairs with opposite energies from the scattering on the obstacle, therefore confirming that the mode conversion at the root of the Hawking effect steadily occurs in our flow. When sending a macroscopic coherent wave from the downstream end of the flume, we measured independently the coefficients α, β and $\tilde{A}$. Their amplitudes agree rather well with results of numerical simulations when the static undulation of the background flow is taken into account.

Acknowledgements : We thank Y. Stepanyants for interesting comments on an early version of this work. We acknowledge support from the University of Poitiers (ACI UP on Wave-Current Interactions 2013-2014), the Interdisciplinary Mission of CNRS (PEPS PTI 2014 DEMRATNOS), and the University of Tours in a joint grant with the University of Poitiers (ARC Poitiers-Tours 2014-2015). We also acknowledge support from the French national research agency (ANR) through the grant HARALAB (N°ANR-15-CE30-0017-04). The water channel was funded by the FEDER 35790-2012.

[1] W. G. Unruh, Phys. Rev. Lett. **46**, 1351 (1981).
[2] C. Barcelo, S. Liberati, and M. Visser, Living Rev. Rel. **8**, 12 (2005).
[3] S. J. Robertson, J. Phys. B: At. Mol. Opt. Phys. **45**, 163001 (2012).
[4] A. Coutant, R. Parentani, and S. Finazzi, Phys. Rev. D **85**, 024021 (2012).
[5] G. Rousseaux, C. Mathis, P. Maissa, T. G. Philbin, and U. Leonhardt, New J. Phys. **10**, 053015 (2008).
[6] T. G. Philbin, C. Kuklewicz, S. Robertson, S. Hill, F. König, and U. Leonhardt, Science **319**, 1367 (2008).
[7] F. Belgiorno, S. L. Cacciatori, G. Ortenzi, V. G. Sala, and D. Faccio, Phys. Rev. Lett. **104**, 140403 (2010).
[8] O. Lahav, A. Itah, A. Blumkin, C. Gordon, S. Rinott, A. Zayats, and J. Steinhauer, Phys. Rev. Lett. **105**, 240401 (2010).
[9] S. Weinfurtner, E. W. Tedford, M. C. J. Penrice, W. G. Unruh, and G. A. Lawrence, Phys. Rev. Lett. **106**, 021302 (2011).
[10] J. Steinhauer, Nat. Phys. **10**, 864 (2014).
[11] H. S. Nguyen, *et al*, Phys. Rev. Lett. **114**, 036402 (2015).
[12] R. D. Acheson, J. Fluid Mech. **7**, 433 (1976).
[13] A. L. Fabrikant and Y. A. Stepanyants, *Propagation of Waves in Shear Flows* (World Scientific, Singapore, 1998).
[14] J.-C. Nardin, G. Rousseaux and P. Coullet, Phys. Rev. Lett., **102** 12, 124504-1/4 (2009).
[15] A. Coutant and R. Parentani, Phys. Fluids **26**, 044106 (2014).
[16] S. W. Hawking, Nature (London) **248**, 30 (1974).
[17] R. Brout, S. Massar, R. Parentani, and Ph. Spindel, Phys. Rep. **260**, 329 (1995), and Phys. Rev. D **52**, 4559 (1995).
[18] I. Carusotto, S. Fagnocchi, A. Recati, R. Balbinot and A. Fabbri, New J. Phys. **10**, 103001 (2008).
[19] J. Macher and R. Parentani, Phys. Rev. A **80** (2009) 043601.
[20] J. R. M. de Nova, I. Zapata and F. Sols, Phys. Rev. A **89** 043808 (2014).
[21] X. Busch and R. Parentani, Phys. Rev. D **89**, no. 10, 105024 (2014).
[22] D. Boiron, A. Fabbri, P.-É. Larré, N. Pavloff, C. I. Westbrook and P. Zin, Phys. Rev. Lett. **115**, no. 2, 025301 (2015).
[23] J. Steinhauer, arXiv:1510.00621 (2015).
[24] R. Schützhold and W. G. Unruh, Phys. Rev. D **66**, 044019 (2002).
[25] G. Rousseaux, P. Maïssa, C. Mathis, P. Coullet, T. G. Philbin, and U. Leonhardt, New J. Phys. **12**, 095018 (2010).
[26] F. Michel and R. Parentani, Phys. Rev. D **90**, 044033 (2014).
[27] P.-J. Faltot, R. Bellanger, J.-M. Mougenot and G. Rousseaux, XIIIèmes Journées Nationales Génie Côtier Génie Civil (2014). *http* : *//www.paralia.fr/jngcgc/*13_10_*faltot.pdf*
[28] L.-P. Euvé, F. Michel, R. Parentani and G. Rousseaux, Phys. Rev. D **91**, 024020 (2015).
[29] G. Jannes, P. Maïssa, T. G. Philbin, and G. Rousseaux, Phys. Rev. D **83**, 104028 (2011).
[30] M. W. Dingemans, *Water Wave Propagation Over Uneven Bottoms* (World Scientific, Singapore, 1997).
[31] W. G. Unruh, Lect. Notes Phys. **870**, 63 (20013).
[32] W. G. Unruh, Phil. Trans. R. Soc. A **366**, 2905 (2008).
[33] S. Weinfurtner, E. W. Tedford, M. C. J. Penrice, W. G. Unruh, and G. A. Lawrence, Lect. Notes Phys. **870**, 167 (2013).
[34] K. M. M. Prabhu, "Window Functions and their Applications in Signal Processing", CRC Press, 2013.
[35] S. Robertson and R. Parentani, Phys. Rev. D **92**, no. 4, 044043 (2015).
[36] X. Busch, F. Michel and R. Parentani, Phys. Rev. D **90**, no. 10, 105005 (2014).
[37] G. Heinzel, A. Rüdiger and R. Schilling, Max Planck Institute (MPI) für Gravitationsphysik, Laser Interferometry and Gravitational Wave Astronomy, 395068 (2002).

SUPPLEMENTAL MATERIAL

Experimental Setup

A beam is produced by an Argon LASER (Spectra Physics 2W), guided by an optical fibre to a cylindrical lens (placed at 1.44 m above the free surface) which formed a LASER sheet. With a LASER power of 0.14 W (after the lens), the power density at the free surface is around 0.05 Wm^{-1}.

We put 50 g of fluorescein in water to have an high concentration (≈ 12 gm^{-3}) in order to obtain a minimum penetration of the LASER sheet into the fluid. Indeed, the LASER light intensity decreases by 90% at 5 mm below the free surface.

The three cameras (Jai CV-M2 CCD), with a resolution of 1600 x 1200 pixels, mounted with a lens of focal length of 50 mm (to have a minimum image distortion), are placed at 2.5 m from the LASER line with a 5° angle with respect to the horizontal (see Fig 7). The visualisation window is therefore 2.16 m wide with a resolution of 0.45 mm. We set the camera lenses with a maximum opening and the shutter speed at 15 ms to capture accurately the LASER line. The thinness of the latter (namely 3 or 4 pixels) allows us to use a sub-pixel detection with an error of 0.1 mm, see [27].

Windowing

The finite length L_I of the spatial integration window has two undesirable effects. First, the Fourier transform of a plane wave has a main lobe with a non-vanishing width, which limits the accuracy in determining the wave-vector k and amplitude A. Second, it also shows side-lobes which produce artefacts in the correlation functions. At fixed L_I, the magnitude of these effects depend on the shape of the window function, which must be suitably chosen to minimize the artefacts while keeping a good accuracy on k and A. We found that a convenient choice is the Hamming window [37], which strongly suppresses the amplitude of the first side-lobes at the expense of multiplying the width of the main one by two with respect to a rectangular window. As shown in Fig. 8, this suppression efficiently erases the artefacts which are clearly visible with a rectangular window.

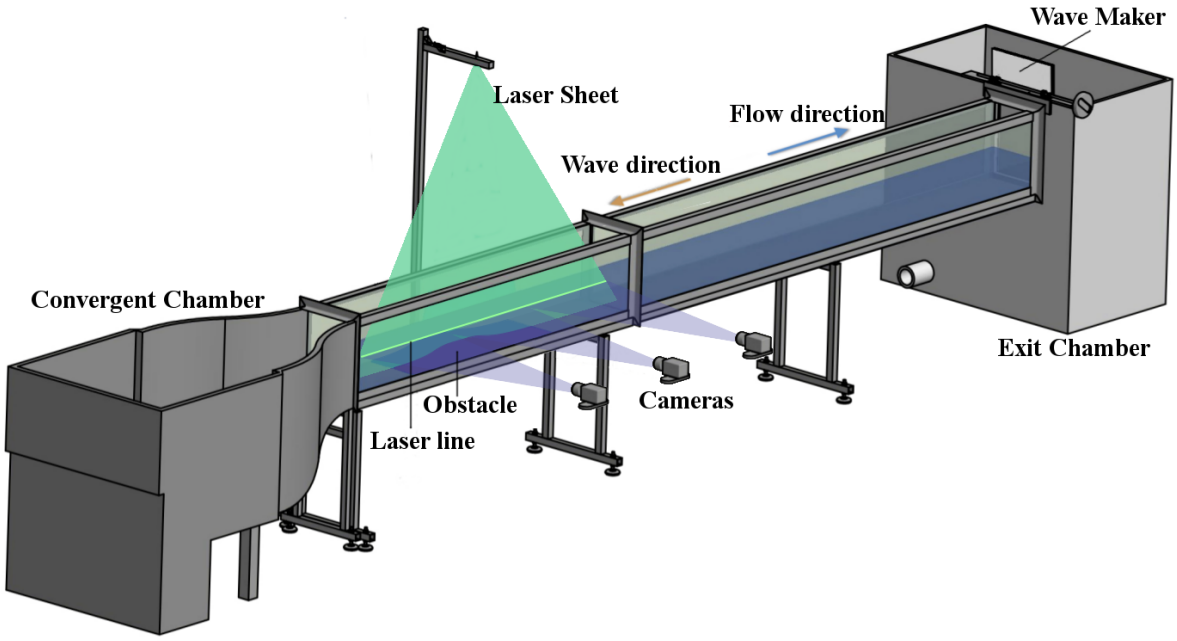

FIG. 7. A sketch of the experimental setup for measuring free surface deformation. The flow goes from left to right, as indicated by the blue arrow, while the incident mode I sent by the wave maker goes in the opposite direction, see brown arrow.

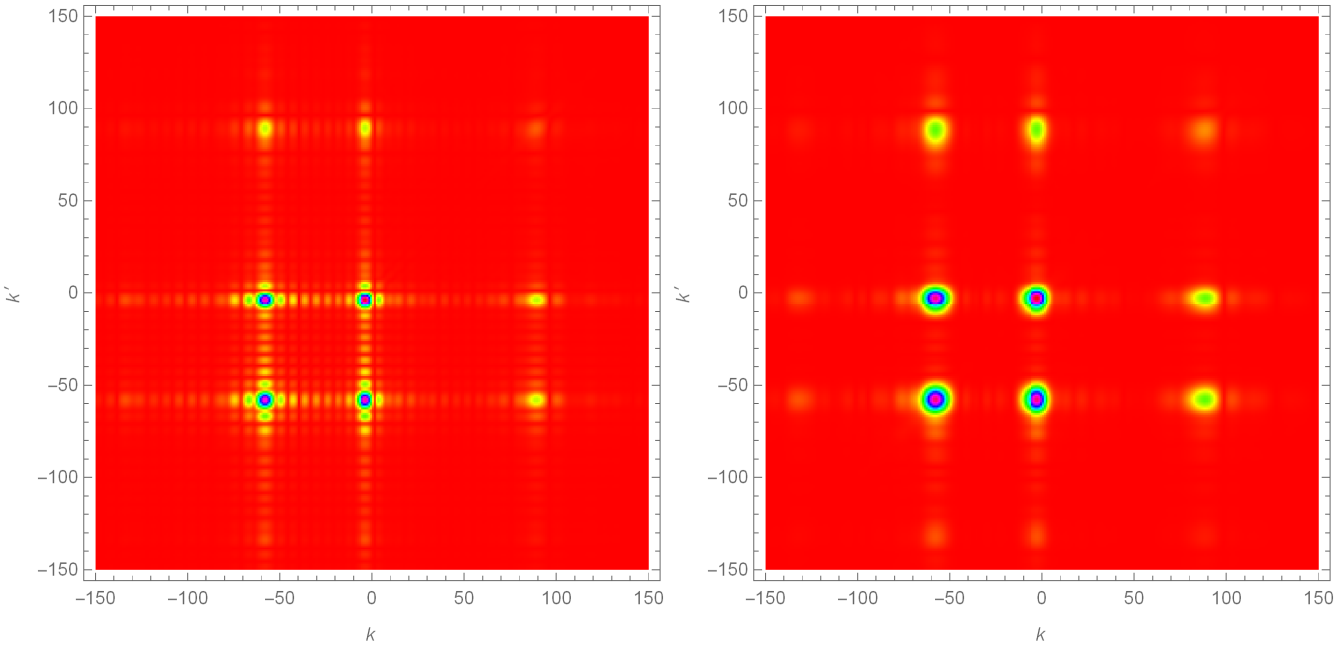

FIG. 8. Comparison of the two-point correlation function $G_2(\omega; k, k')$ of Eq. (3) evaluated using a rectangular window (left) and a Hamming window (right) over $x \in [0.45\mathrm{m}, 1.45\mathrm{m}]$, for the case when an incident wave of angular frequency $\omega = 2.5$ Hz. k and k' are expressed in m^{-1}.